Supplemental Materials and Methods

A. Detailed Methods

B. Online Tables

C. Online Figures

D. Supplemental References

A. Detailed Methods

Myocardial infarction model and in vivo phenotyping.

Adult female C57BL/6N mice were randomized to post myocardial infarction (post-MI) remodeling for either 4 weeks or 8 weeks (4pMI or 8pMI, respectively) or sham procedure. The left anterior descending coronary artery (LAD) was proximally ligated. Cardiac remodeling was characterized in vivo by rodent echocardiography (Vevo2100 VisualSonics, Toronto) and by normalized heart weight. All animal procedures were reviewed and approved by the Institutional Animal Care and Use Committee at University Medicine Goettingen and by veterinarian state authority LAVES (Niedersächsisches Landesamt für Verbraucherschutz und Lebensmittelsicherheit) in compliance with the humane care and use of laboratory animals. Mice were treated 3 days before, during and 3 days after surgery by buprenorphin (0.06 µg/g body weight s.c.) and metamizol (1.33 mg/ml by drinking water), and during surgery with 2% isoflurane in O_2 ventilated with a tidal volume of 0.15 ml (150 strokes/min). A left lateral thoracotomy was performed, and the left anterior descending coronary artery (LAD) was proximally ligated with a 9-0 polyamide suture. Myocardial infarction was immediately confirmed as permanent distal tissue blanching through a binocular operating microscope, and infarct size estimated (0-100%). Sham operated animals underwent the same procedure, except occlusion of the LAD. The chest was closed, the lungs were inflated, and the animal monitored until spontaneous, regular breathing occurred and daily following surgery.

Pre- and postoperatively mice were characterized by echocardiography (Vevo2100 VisualSonics, Toronto) using a 30 Hz transducer (MS-400 MicroScan Transducer, Linear Array Technology). Left ventricular dimensions were determined by parasternal long axis and short axis views. Echocardiographic dimensions reported include terminal observation time points (Online Figure III) for ejection fraction (EF) and diastolic cross-section area (Area, d) calculated from consecutive parasternal left ventricular contraction cycles. In addition, post-MI scar

thinning of the anterior free wall was confirmed by measuring anterior wall thickness (AWTh,d) and confirmed as significant decrease versus sham (data not shown). At the time of euthanasia wet total heart weight was determined and normalized to body weight (HW/BW). Based on previous experience with the same background strain, same LAD ligation protocol, and histological analysis of transversal heart sections (data not shown), infarct sizes approximate 35% on average at 8pMI.[1] Therefore, infarct size was again estimated (0-100%) during organ extraction and only hearts with consistent infarct sizes were used for further analysis.

Female as compared to male mice were reported to show better post-MI survival attributed to reduced mortality,[2, 3] less dilative remodeling,[2, 3] a reduced incidence of cardiac rupture,[4, 5] and better LV systolic function.[3, 4, 6] As our study investigated early versus late post-MI remodeling mechanisms during progressive heart failure development, female mice were considered advantageous in order to establish continuous uniform data samples at multiple investigatory levels in a relatively stable post-MI population with predictable HF behavior. As expected, the cardiac and cellular pathology each showed significant post-MI progression (Online Figures III and IV) confirming a relatively uniform disease substrate.

Myocyte preparation for live cell imaging

Isolated mouse hearts were Langendorff perfused with a Ca^{2+} free oxygenated Krebs buffer followed by collagenase type II containing solution (2 mg/ml, Worthington Biochemical Corporation). Ventricular cardiomyocytes were plated on laminin coated glass cover slips for subsequent imaging studies. For cardiac myocyte isolation mice were euthanized, hearts were quickly extracted and the aorta connected to a 21G cannula. The heart was Langendorff perfused with Ca^{2+} free oxygenated Krebs solution (in mmol/L: NaCl 120.4, KCl 14.7, KH_2PO_4 0.6, Na_2HPO_4 0.6, $MgSO_4$ 1.2, HEPES 10, $NaHCO_3$ 4.6, taurin 30, 2,3-butanedione-monoxime 10, glucose 5.5, pH 7.4) at 37°C for 4 mins. Perfusion was switched to collagenase type II

containing solution for 9 mins. Following digestion, left and right ventricle tissue was dissected into 1 mm^3 pieces in collagenase containing buffer, whereas all post-MI scar tissue was carefully excised and discarded. Digestion was stopped by the Krebs buffer containing 10% bovine calf serum (HyClone Laboratories) and 12.5 µM $CaCl_2$. Isolated myocytes were washed at least two times before plating on laminin (mouse laminin, BD Biosciences) coated glass cover slips (Ø 42 mm, Thermo Scientific) at a nominal density of 1500 cells/cm^2.

Selection of membrane probe for live cell STED imaging

We used STED nanoscopy to image the continuous TT membrane network in living cardiac myocytes stained with fluorescent membrane dyes. In pilot studies, we tested several dyes of which di-8-ANEPPS resulted in bright signals of TT membranes in stably quiescent myocytes during STED imaging (Figure 1), an important prerequisite for super-resolution live cell imaging. However, myocytes stained with previously described derivatives of fluorescently labeled phosphoethanolamines (Atto647N-PE and Atto647N-PE1) or sphingolipids (Atto647N-SM)[7], or di-4-ANEPPS showed different degrees of dye internalization and/or contracted irregularly. Therefore, we performed all imaging experiments using a myocyte staining protocol based on the lipophilic fluorescent probe di-8-ANEPPS (50 µM, Molecular Probes) for 10 mins at room temperature followed by two washing steps with Krebs buffer. Myocytes were randomly selected and imaged in fresh physiological Krebs buffer on laminin coated coverslips.

STED microscopy, image acquisition, and image analysis

Please also refer to the Methods section of the main manuscript.

Image processing for analysis of TT dimensions by FWHM

Prior to quantitative analysis, all images where deconvolved using a Wiener filter and the respective point spread function as kernel (Matlab R2009b; The MathWorks). Next, a 2D Gauss

function was fitted to the fluorescence signal distribution of unconnected (“free”) transversal TT cross-sections (Figure 1B, rightward images, marked by arrowhead). The function used different variances along both orthogonal axes. The orientation of the two perpendicular axes was fixed and aligned with the two principal cell axes during fitting (longitudinal or transversal). Cell orientation was determined from transmitted light images as shown in Figure 1B. Accordingly, full width at half maximum (FWHM) was determined along the longitudinal (X) and the transversal (Y) axis from the fitted 2D Gauss data. The corresponding ellipse area was calculated from the measured X and Y diameters for each TT cross-section by formula: $A = \pi (0.5 \cdot X) \cdot (0.5 \cdot Y)$. While FWHM depends on the microscope point-spread-function, we used regular nanobead calibrations (20 nm) to ensure stability between measurements.

Automated TT cross-section analysis by contours and data processing

Contour lines were computed with a resolution of 120 points per curve using the Matlab command *contourc* for individual TT cross-sections using a 50% threshold of the maximal pixel fluorescence intensity in deconvolved images. Using the center of mass, all contour lines of a given TT population were superimposed in space (X, Y) and presented as 2D probability histogram (color coded, contour procedures described with Figure 2). In addition, the circumferences of TT contours are reported as mean data by Tables 1 and 2 and Online Tables I and II.

Radius analysis from individual TT contours

In addition, we determined the radius size of individual TT cross-sections as the median radius of the corresponding contour. Median distributions are presented for different imaging modes or treatment groups. Using a non-parametric test (Mann-Whitney) changes in median distribution of the radius sizes were accepted for $p<0.05$. Furthermore, two-peak Gaussian fitting was used to document heterogeneous changes in TT radius sizes 8 weeks post-MI (8pMI).

Skeleton detection and spatial orientation analysis

2D skeletons of continuous TT networks were extracted from STED images by ImageJ (imagej.nih.gov) and Fiji (pacific.mpi-cbg.de). A statistical region-merging algorithm was applied, the data were binarised by thresholding of identical intensity percentiles, and continuous ("intact") skeleton data were extracted from the binarised images.[8] TT skeletons were next analyzed with a Fiji plug-in algorithm ("directionality") to quantify the spatial orientations of individual network components from continuous TT networks. We computed histograms to assess the orientation probability of TT network components in 2D space and corresponding to the two principal cell directions (longitudinal versus transversal) based on local gradient orientations detected by a 5x5 Sobel filter.[9]

Cell size and co-immunofluorescence measurements

Cell area, length and width were documented (Online Figure IV). To determine myocyte dimensions, a fraction of the cells were fixed immediately after isolation with 4% PFA (5 mins at room temperature) following adherence on laminin coated coverslips (mouse laminin, BD Biosciences). Following additional PBS washing steps (pH 7.4, $CaCl_2$ and $MgCl_2$ free, GIBCO) cells were embedded in mounting medium (ProLong Gold Antifade Reagent, Invitrogen). Fixed samples were documented by transmitted light mode (Zeiss LSM 710, Jena, Germany). Using ImageJ (imagej.nih.gov) the myocyte surface border/contour, area, length and width were determined as presented in Online Figure IV.

For immunofluorescence studies cells were permeabilized (0.2 % Triton X-100, 10 % bovine calf serum in PBS) for 1 h after the PBS washing steps. Cells were incubated over night with the following primary antibodies and dilutions: rabbit anti-junctophilin-2 1:500 (Invitrogen 40-5300), rabbit anti-caveolin-3 1:500 (Abcam ab2912), and mouse anti-RyR2 1:500 (Thermo Fisher Scientific MA3-916). After three washing steps, cells were incubated for 1.5 hrs with the following secondary antibodies and dilutions: anti-mouse Alexa Fluor 514 1:1000 (Invitrogen A31555) and anti-rabbit Alexa Fluor 633 1:1000 (Invitrogen A21071). Samples were imaged

using a Zeiss LSM 710 using a 63x 1.4 NA oil objective and a pixelsize of 80 nm. Exication (ex.) and detection (det.) settings were as follows: Alexa Fluor 514 ex. 514 nm, det. 520 – 620 nm; Alexa Fluor 633 ex. 633 nm, det. 640 – 740 nm.

Analysis of T-tubule associated protein localizations

The signal distribution of Cav3, RyR2, or Jph2 immunostained cardiomyocytes was analyzed by Fast Fourier transformation (FFT) using ImageJ (imagej.nih.gov). The power spectrum of each image was computed individually and the average power spectra for the indicated treatment groups (sham, 4pMI, 8pMI) are shown as a function of spatial frequency.[10] Data are presented as Online Figure VII.

Combined confocal Ca^{2+} and T-tubule imaging in transverse and longitudinal directions. Using a LSM 710 confocal microscopy system (Carl Zeiss; Jena, Germany) and a 63x 1.4 NA oil objective, line scan imaging of cardiomyocytes was performed each in the transversal and longitudinal cell direction. Di-8-ANEPPS (10 µM, 10 min) and fluo-4 AM (10 µM, 30 min) signals were recorded by longitudinal scanning at room temperature according to the protocol described by Louch et al.[11] Since the LSM 710 system allows for a high spectral separation, di-8-ANEPPS (excitation: 458 nm, detection: 550 - 740 nm) and fluo-4 AM (excitation: 488 nm, detection: 490 – 540 nm) signals were separately recorded. We used a modified protocol using a 20 µm scan line (100 pixels) each for transversal and longitudinal directions to correlate functional measurements with directional post-MI T-tubule component changes (which have been independently documented by STED imaging). Image analysis was performed with ImageJ. The spatially averaged fluo-4 line scan signal was thresholded at 50% intensity, to analyze temporal deviations from F50 as described by Louch et al.[11] For transversal line scan imaging, representative T-tubule and Ca^{2+} signals are presented in Figure 5C. Temporal deviations (standard deviation) from F50 are documented as the dyssynchrony index.

Protein analysis

Isolated cardiac myocytes were used for biochemical analysis, pelleted by sedimentation for 8 min, immediately snap-frozen and stored at -80°C. Cells were homogenized using a 0.5 - 1.0 ml glass/Teflon Potter-Elvehjem homogenizer (300 rpm; 10-20 strokes) in homogenization buffer consisting of: 50 mmol/L Hepes, KOH titrated pH 7,4, 300 mmol/L sucrose, 150 mmol/L NaCl, 0.5 % (v/v) Triton X-100, protease and phosphatase inhibitor mix (Roche). To remove insoluble debris, lysates were spun at 8,000 g for 15 mins at 4°C. The supernatant was aliquoted and immediately snap-frozen. For Western blots 20 µg of protein were resolved by SDS-PAGE using a 4-12% gradient gels (Novex, Life Technologies) and transferred to Protean nitrocellulose membranes (Whatman), blocked in 5% (w/v) nonfat milk in Tris-buffered saline with 0.05% (v/v) Tween 20, and detected using the following antibodies and dilutions: anti-junctophilin-2 1:1000 (Invitrogen 40-5300), anti-caveolin-3 1:2000 (Abcam ab2912), anti-RyR2 1:2500 (Prestige, Sigma), anti-GAPDH 1:40,000 (Biotrend 5G4MAB6C5). After three washes, membranes were incubated with horseradish peroxidase labeled anti-rabbit or anti-mouse IgG 1:10,000 for 1 h at room temperature (GE Healthcare NA934 & NXA931), washed three times and developed with chemiluminescent reagent (Immobilon Western Chemiluminescent HRP substrate, Millipore). The intensity of the signal was collected using a Kodak Imaging Station 4000R. Band densitometry analysis was performed using Carestream MI Software V.5.0.3. Data are reported as normalized change compared to sham.

Computational modeling of local Ca^{2+} release during heterogeneous CRU spacing

Local CRU Ca^{2+} sparks and cell-wide Ca^{2+} transients were investigated using the mathematical model of Williams et al. 2011,[12] which includes spatial nanodomain determinants of individual CRU organization and a realistic number of 20,000 release sites. The whole-cell model is fully stochastic including Ca^{2+} spark behavior, and reproduces the systolic $[Ca^{2+}]_i$ transient

throughout a propagated action potential activating L-type Ca^{2+} channels (LCC) at the surface membrane and at TTs. The LCC current elevates $[Ca^{2+}]_i$ locally in the "subspace" compartment between the TT and terminal SR membrane, which is greatly amplified when RyR2 clusters are activated by locally elevated subspace $[Ca^{2+}]_i$ as occurs during CICR. The recently developed mathematical model examines how local subspace $[Ca^{2+}]_i$ signaling changes between control and HF conditions by implementing previously observed (published) changes in ion transport proteins: fast and slow K^+ currents (I_{to} and I_K) were reduced by 30%; NCX protein expression was increased by 100%;[13] SR Ca^{2+} ATPase (SERCA2a) protein was decreased by 30%;[14] and RyR2 Ca^{2+} sensitivity was increased by 50% to mimic increased activity from chronic hyperphosphorylation.[1] In addition, “orphaning” of RyR2 clusters during heart failure during heterogeneous changes of individual TT structures (as reported by this study) was modeled as a 30-fold increase in subspace volume for only 25% of CRUs and as a reduction of the transversal TT component leading to a 20% decreased total membrane capacitance. The increased subspace volume of diseased CRU release sites are the equivalent of moving individual TT membranes 300 nm away from associated CRU release sites.

Statistics

Data are presented as mean ± SEM unless indicated otherwise. Differences between groups were tested for statistical significance using the unpaired 2-tailed or paired Student’s t-test as appropriate. The nonparametric Mann-Whitney test was used to determine significant differences in median TT radius distributions. P values less than 0.05 were considered significant.

B. Supplemental Tables

Online Table I

T-tubule dimensions at subsurface locations in untreated control myocytes imaged by confocal versus STED mode.

Imaging mode	Diameter X (nm)	Diameter Y (nm)	Area (1000 nm^2)	Circumference (nm)
Confocal	273.1 ± 2.7	266.1 ± 2.1	57.2 ± 0.7	945.3 ± 6.7
STED	206.0 ± 3.5 *	194.6 ± 2.7 *	31.8 ± 0.7 *	708.6 ± 9.8 *

TT cross-sections at subsurface locations were directly compared by confocal versus STED mode less than 3 μm from the surface membrane. TT diameters represent FWHM measured by automated 2D Gauss analysis corresponding to X (longitudinal) and Y (transverse) orientations (as given by Figure 1A). Circumference was determined by automated contour analysis (see Online methods). Data represent paired measurements; *$p<0.001$ vs. confocal imaging; mean ± SEM from 182 TT cross-sections and 55 cells.

Online Table II

T-tubule dimensions at subsurface locations during HF development.

Treatment group	Diameter X (nm)	Diameter Y (nm)	Area (1000 nm^2)	Circumference (nm)
Sham [a]	201.0 ± 2.0	190.5 ± 1.8	30.3 ± 0.4	656.0 ± 5.6
4pMI [b]	199.5 ± 2.7 n.s.	190.3 ± 2.6 n.s.	29.8 ± 0.5 n.s.	649.4 ± 7.5 n.s.
8pMI [c]	214.7 ± 3.3 * †	205.7 ± 3.3 * †	35.0 ± 0.8 * †	701.0 ± 10.4 * †

TT cross-sections at subsurface locations were imaged by STED less than 3 µm from the surface membrane from randomly selected cells of the indicated treatment groups. TT diameters represent FWHM measured by automated 2D Gauss analysis corresponding to X (longitudinal) and Y (transverse) orientations. Circumference was determined by automated contour analysis. Data represent unpaired measurements; *$p<0.05$ vs. sham; †$p<0.05$ vs. 4 weeks post-MI; n.s., not significant; mean ± SEM from the following number of TT cross-sections/cells per treatment group: [a] sham 683/92, [b] 4 weeks post-MI (4pMI) 343/61, and [c] 8 weeks post-MI (8pMI) 253/48.

Online Table III

Length of the T-tubule network, its components, and post-MI changes.

Treatment group	Total network length ($\mu m/\mu m^2$)	Transversal component length ($\mu m/\mu m^2$)	Longitudinal component length ($\mu m/\mu m^2$)	Oblique component length ($\mu m/\mu m^2$)
Sham [a]	0.38 ± 0.02	0.020 ± 0.001	0.024 ± 0.002	0.018 ± 0.002
4pMI [b]	0.52 ± 0.04 *	0.020 ± 0.002 n.s.	0.045 ± 0.006 *	0.026 ± 0.002 *
8pMI [c]	0.50 ± 0.03 *	0.021 ± 0.003 n.s.	0.032 ± 0.003 †	0.028 ± 0.002 *

Length normalized to area of the T-tubule network and its longitudinal, transversal, and oblique components. We report the total length normalized to analyzed ROI area for each component ($\mu m/\mu m^2$) as well as changes after myocardial infarction. Longitudinal (0°) and transversal (90°) T-tubule components represent ± 3° large bins. Oblique components represent the sum of +45° ± 3° and -45 ± 3° bins. Data represent unpaired measurements; *$p<0.01$ vs. sham; †$p<0.05$ vs. 4 weeks post-MI; n.s., not significant; mean ± SEM from the following number of cells per treatment group: [a] sham 23, [b] 4 weeks post-MI (4pMI) 19, and [c] 8 weeks post-MI (8pMI) 19.

Online Table IV

T-tubule changes in ventricular myocytes reported by experimental studies or investigation of patient samples

A. Experimental studies of heart disease models and associated T-tubule changes (in chronological order)

Disease model	Time point studied	T-tubule changes	References
Pacing-induced canine HF	~5 weeks after pacing	Regional loss, reduced density	He, 2001 [15]
Pacing-induced canine HF	~6 weeks after pacing	Regional loss	Balijepalli, 2003 [16]
Spontaneously hypertensive rat with congestive HF	at 19.2 months age	Reduced transversal network component, chaotic network reorganization	Song, 2006 [10]
Mouse post-MI HF	1 week or 3 weeks after MI	Regional disorganization; 1 week "somewhat"; 3 weeks: "marked"	Louch, 2006 [11]
Pig post-MI HF	6 weeks after MI	Regional loss, reduced density	Heinzel, 2008 [17]
Rat post-MI end-stage HF	16 weeks after MI	Regional loss, reduced density	Lyon, 2009 [18]
Rat heterotopic abdominal heart transplantation	4 weeks of cardiac unloading	Network reorganization, loss of surface connections	Ibrahim, 2010, [19]
Rat aortic banding hypertrophy and HF	9.2 weeks hypertrophy; or 9.9 weeks HF	Regional loss, different degrees of TT loss from "discrete" to "dramatic"	Wei, 2010 [20]
Inducible cardiac-specific knockdown of Junctophilin-2	1 week after knockdown induction, adult heart	Regional loss, increased CRU spacing and loss of CRU junctions	van Ort, 2011 [21]
PI3K p110α/β double knockout	5 weeks age	Regional loss	Wu, 2011 [22]
Rat post-MI HF	4 weeks post-MI	Reduced TT density	Kemi, 2011 [23]
Canine dyssynchronous HF	6 weeks after intervention	Sparse at cell center; longitudinal increase	Sachse, 2012 [24]

B. Studies of patient samples from diseased hearts and associated T-tubule changes (in chronological order)

Disease studied	Sample studied	T-tubule changes	References
Different HCM samples	Fixed biopsy sections	Loss and dilation of TTs	Maron, 1975 [25]
End-stage DCM	Fixed tissue sections	Proliferation and dilation	Schaper, 1991 [26]
End-stage DCM	Fixed tissue cryosections	Regional loss and dilations	Kostin, 1998 [27]
End-stage DCM, ICM	Fixed tissue sections	Increase in size and longitudinal elements	Kaprielian, 2000 [28]
End-stage DCM, ICM	Isolated living myocytes	Normal density, occasional dilation	Louch, 2004 [29]
End-stage tachycardia HF	Fixed tissue sections	Reorganization, increase oblique TTs	Cannell, 2006 [30]
End-stage DCM, HCM, ICM	Isolated living myocytes	Regional TT loss, reduced TT density	Lyon, 2009 [18]
End-stage DCM	Fixed tissue sections	Loss transverse TTs, increase oblique TTs	Crossmann, 2011 [31]

Abbreviations: DCM, Dilated Cardiomyopathy; HCM, Hypertrophic Cardiomyopathy; ICM, Ischemic Cardiomyopathy.

C. Online Figures

Online Figure I

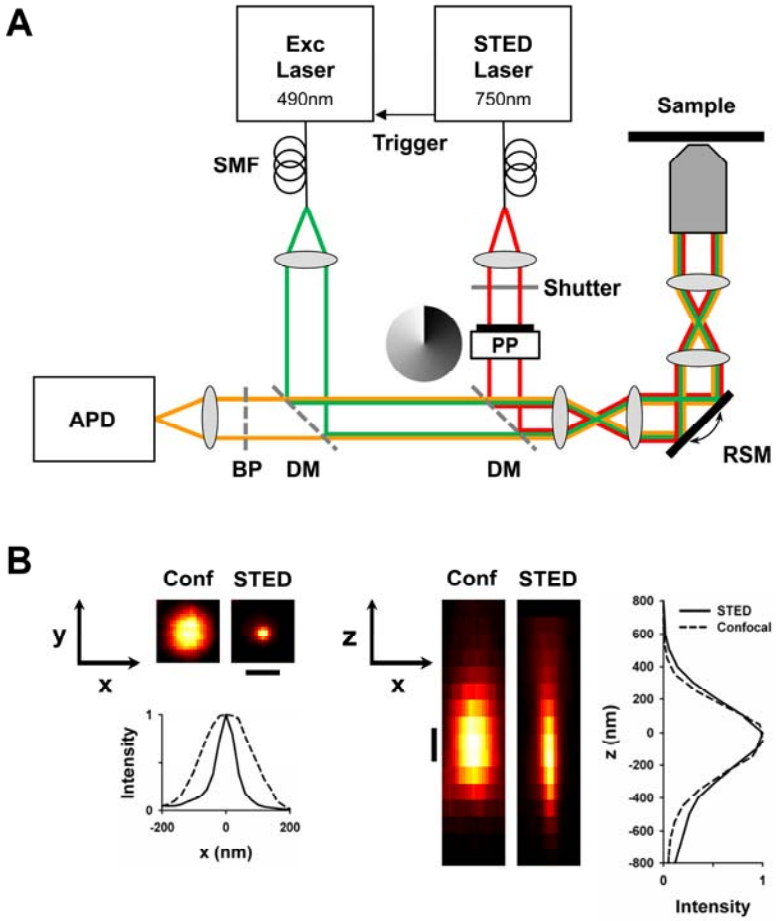

Confocal

	FWHM Mean ± SD	n
x	191 ± 11	10
y	203 ± 21	10
z	455 ± 21	10

STED

	FWHM Mean ± SD	n
x	58 ± 8	25
y	52 ± 8	25
z	479 ± 112	20

Online Figure I

Imaging principles of STED nanoscopy.
A, Using an inverted microscope (Leica) custom-modified for beam scanning and STED microscopy, the STED beam is switched ON/OFF by a shutter for super-resolution versus confocal imaging, respectively. APD, avalanche photo diode; DM, dichroic mirror; Exc, excitation laser; SMF, single mode fiber; Trigger, synchronizes STED and excitation laser pulses; PP, phase plate; RSM, resonant scanning mirror.
B, Nanobead (20 nm) measurements document significantly reduced focal spot size below the diffraction barrier for STED. *Left*: *xy* intensity projection of individual data from n nanobeads (given by tables) showing lateral signal spread for confocal and STED modes, and average point-spread-functions. *Right*: *xz* intensity projection for confocal and STED nanobead measurements, and average point-spread-functions. *Bottom*: Tables summarizing average FWHM for confocal and STED modes, and numbers of measured nanobeads. Conf, confocal; scale 200 nm.

Online Figure II

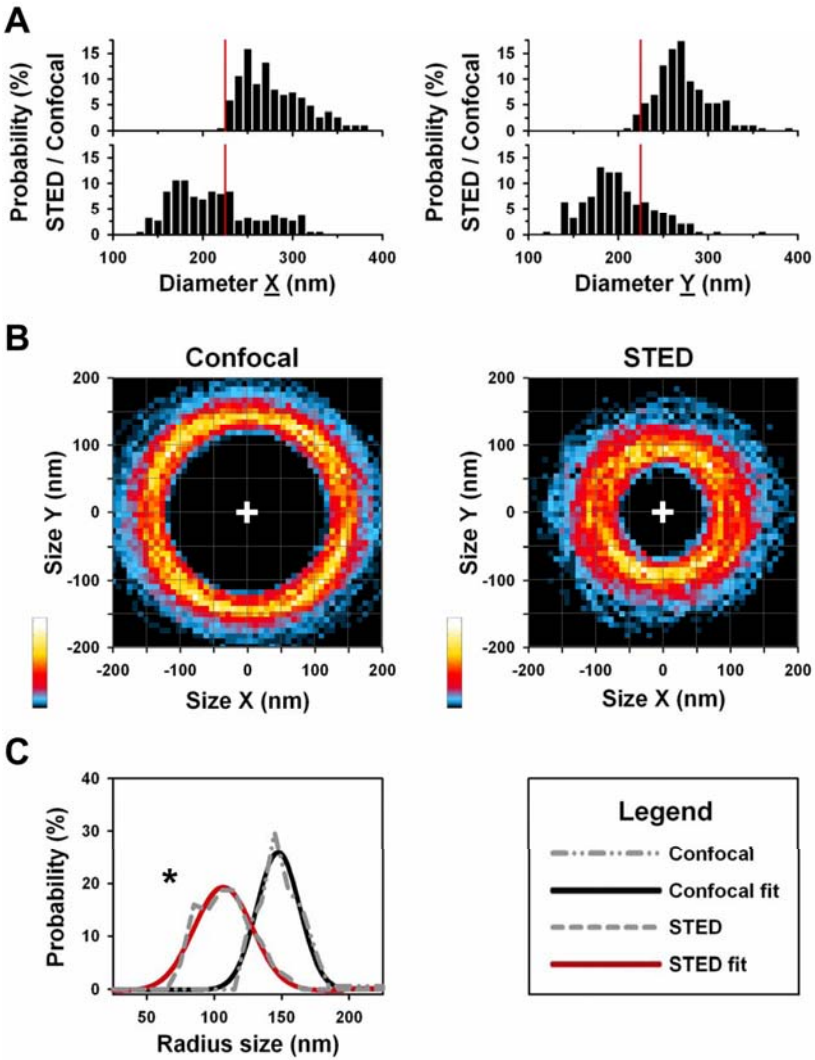

Online Figure II

STED imaging of TT cross-sections at "submembrane" locations less than 3 µm from the cell surface of living control myocytes.

A, Histograms of the following TT cross-section dimensions: diameter X, *left*; diameter Y, *right* each from confocal (*upper*) versus STED (*lower*) data imaged less than 3 µm from myocyte surface membrane. Diameters represent full width at half maximum (FWHM) each for longitudinal (X) and transversal (Y) directions, determined by fitting a 2D Gaussian function to the fluorescence intensity distribution (see Online methods). Vertical red line marks 220 nm, the confocal resolution limit. **B**, Same TT cross-sections (n = 182) as in (**A**) were analyzed by automated contour algorithm using a 50% intensity threshold (see Online methods). Contour data are presented as 2D probability histogram each for confocal and STED mode documenting differences in distribution. Contours are centered by origin (indicated by '+'). Colors indicate pixel probabilities as given by look-up-table. **C**, STED versus confocal imaging near the surface membrane results in different median distributions of radius sizes (grey dashed lines; *p<0.05, non-parametric Mann-Whitney test). Radius sizes were determined from individual TT cross-sections by contour analysis (see methods). In addition, Gaussian fitting confirmed a left-shifted and wider distribution of radius sizes for STED (red line) versus confocal (black line) mode confirming faithful detection of individual TT structures. Mean data are summarized in Online Table I.

Online Figure III

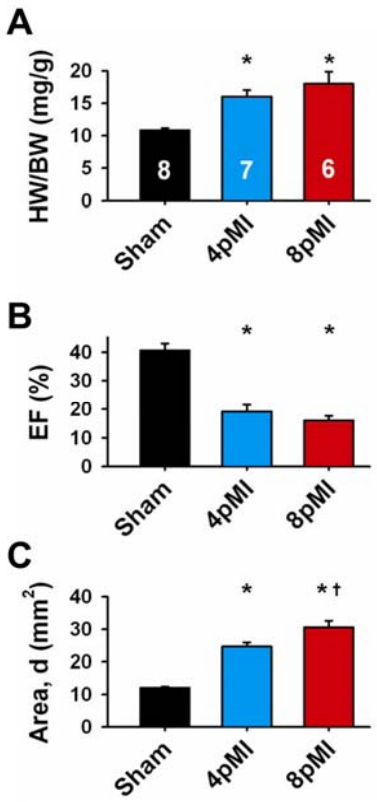

Online Figure III

In vivo cardiac phenotype and progressive remodeling after myocardial infarction.

A, Heart weight normalized to body weight was significantly increased at 4pMI and 8pMI. **B**, Echocardiographic measurements showed a significant decrease in ejection fraction at 4pMI and 8pMI. **C**, Left ventricular end-diastolic cross-section area (Area, d) was significantly increased at 4pMI and 8pMI. Bar graphs represent unpaired measurements; *$p<0.05$ vs. sham; †$p<0.05$ versus 4pMI; means ± SEM; animal numbers are indicated in (**A**) and reflect only hearts used for isolated cell analysis.

Online Figure IV

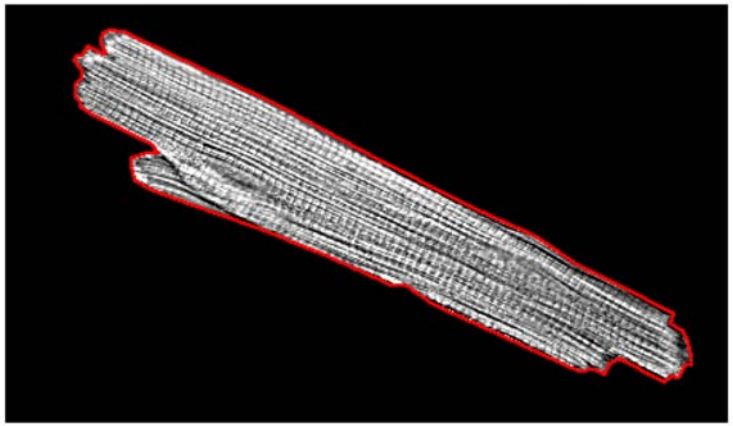

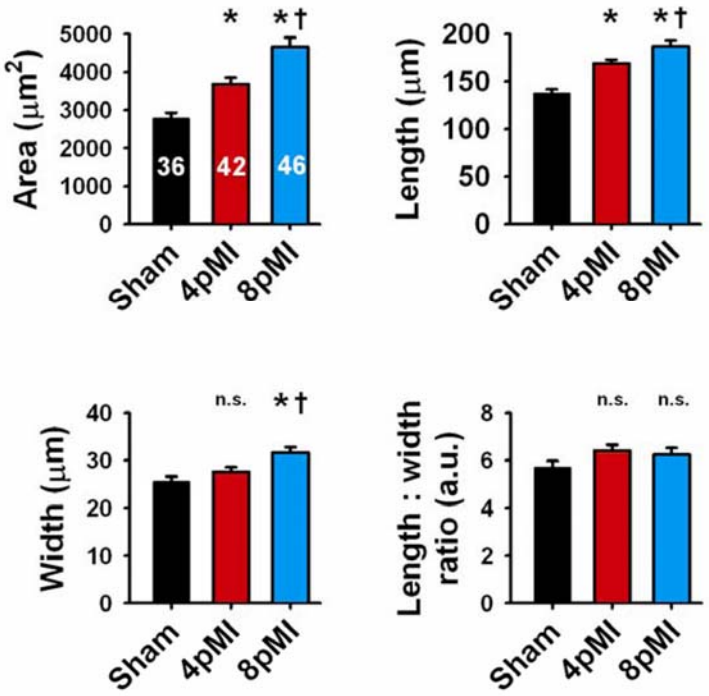

Online Figure IV

Myocyte dimensions increase progressively during HF development following myocardial infarction.
Top: Example cell from a sham heart. Myocyte dimensions were determined by automated surface/contour analysis (red line) from randomly selected, laminin plated, and fixed cells of different treatment groups by transmitted light imaging. We used freely available ImageJ software for analysis (http://rsbweb.nih.gov/ij).
Bar graphs document progressive increase of cell dimensions by area, length, width, and ratio length:width at 4pMI and 8pMI versus sham cells. Numbers of cells are indicated in first bar graph. Symbols: *p<0.05 vs. sham; †p<0.05 vs. 4pMI; n.s., not significant.

Online Figure V

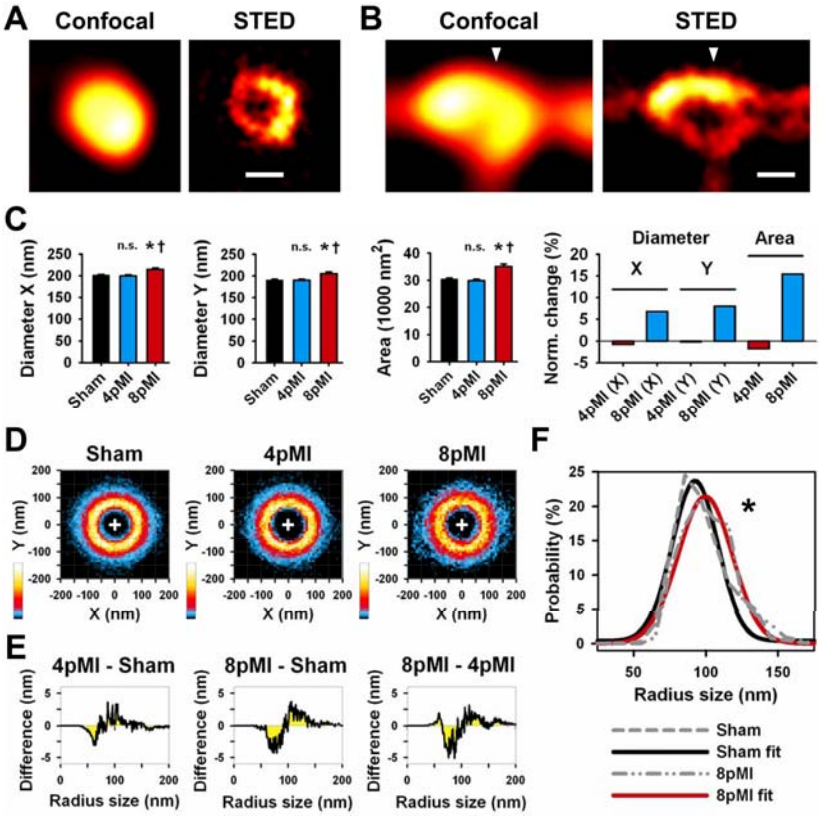

Online Figure V

STED imaging of TT cross-sections at "subsurface" locations less than 3 µm from the cell surface during HF development.

A, Confocal versus STED image examples of the same enlarged subsurface TT cross-section at 8pMI. Scale 200 nm. **B**, Confocal versus STED images of the same super-enlarged TT cross-section membrane complex at 8pMI (arrowhead: position of striation). Scale 200 nm. **C**, Longitudinal (X) and transversal (Y) diameters at subsurface locations were determined as FWHM from TT cross-sections (see methods). Bar graphs summarize mean TT diameters X and Y, and cross-section area; *right*: percent change in TT cross-section dimensions normalized to sham. *p<0.05 versus sham; †p<0.05 versus 4pMI; n.s., not significant. **D**, 2D probability histograms of contour data from subsurface TT cross-sections of the indicated treatment groups (same TT cross-sections as in **C**). TT cross-sections were analyzed by automated contour algorithm (see methods). Colors represent highest (white) versus lowest (black) contour pixel probabilities as indicated by look-up-table. **E**, Difference integrals were calculated from averaged data of individual TT radius sizes and presented as difference between the indicated treatment groups. Compared to sham, a decrease of small versus an increase of large TT radius sizes occurred during HF development. However, at 4pMI the changes are less pronounced at subsurface compared to deep intracellular locations (see Figure 3F). **F**, Median radius size distributions calculated from individual subsurface TT contours of sham and 8pMI cells (grey dashed lines). The 8pMI distribution is significantly right-shifted (*p<0.05). Furthermore, Gaussian fitting of the 8pMI data (red line) confirmed a rightward shift toward increased radius sizes at 8pMI. However, the changes were less pronounced at subsurface as compared to deep intracellular locations (see Figure 3G). Mean data are summarized in Online Table II.

Online Figure VI

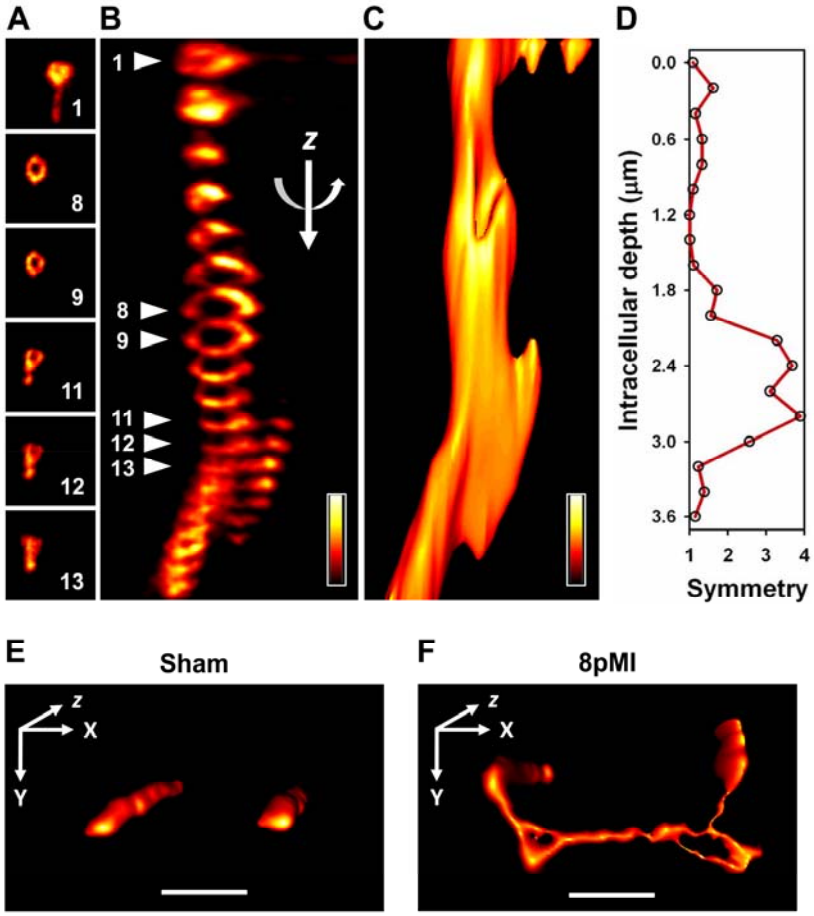

Online Figure VI

Optical sectioning and surface topography of TT substructures.

A, Selected examples of a live cell STED image stack showing TT cross-sections in different imaging depth (*z*); images were processed according to the PSF given by online figure IB. Numbers correspond with indicated *z* positions in (**B**), marked by arrowheads. **B**, 3D side view (90º rotation) of entire TT image stack from the myocyte surface (top) toward the cell center (19 sections every 200 nm). Note membrane evaginations of selected TT cross-sections (planes 1, and 11 and higher). **C**, 3D surface topography further rotated to highlight lower TT section containing membrane evaginations. **D**, Graph showing fold deviation (> 1) from an ideal circular TT cross-section symmetry, determined as the ratio of longitudinal over transversal diameter length by manual contour analysis. Note that TT cross-sections deviating from a circular symmetry (up to 4-fold) correspond with imaging sections containing TT membrane evaginations. **E**, Top view from the cell surface showing two reconstructed transversal TTs at neighboring sarcomere striations from a sham heart; and **F**, at 8pMI two neighboring transversal TTs continuously connected through a longitudinal TT element and super-enlarged cross-sections resulting in a complex, abnormal membrane morphology (see also Figure 3B, Figure 4 and results section for analysis of super-enlarged TT cross-sections). Sham and 8pMI surface reconstructions represent 7 image planes every 300 nm using the indicated 3D orientation; scale 1 µm.

Online Figure VII

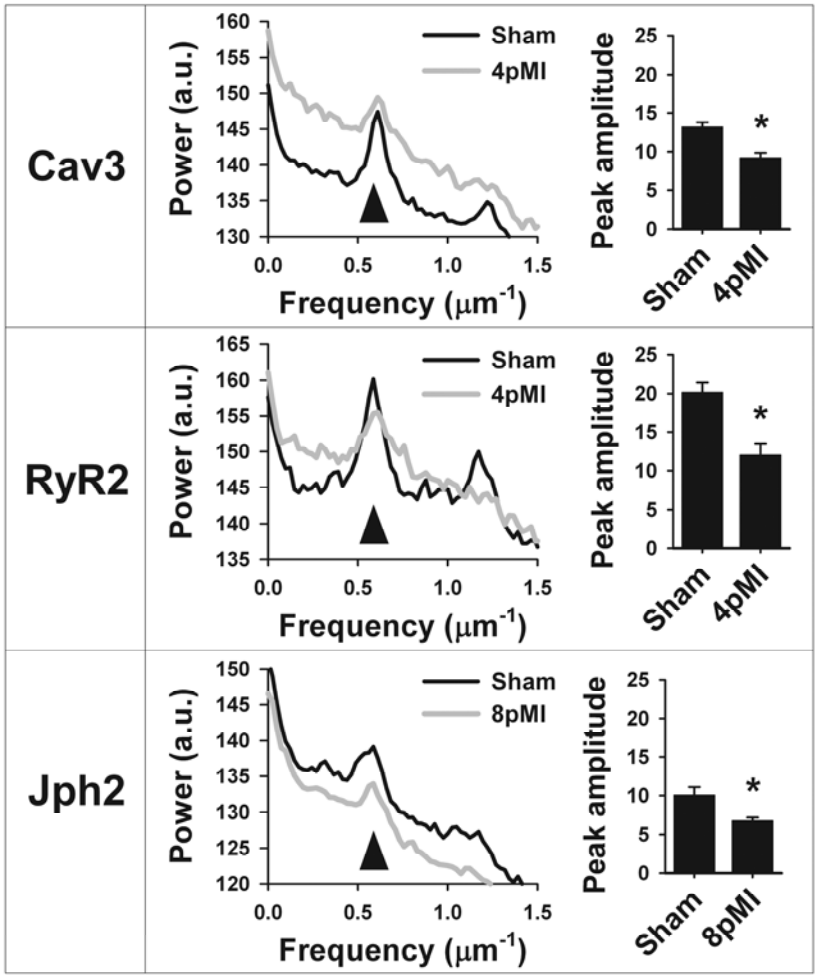

Online Figure VII

Analysis of TT associated protein clusters by confocal imaging of immunostained LV cardiomyocytes from post-MI or sham hearts.

Using Fast Fourier transformation, the striation associated periodic signal amplitude represented by the first spatial frequency (at 0.55 μm^{-1}) was analyzed each for the indicated Cav3, RyR2, and Jph2 cluster changes post-MI. Bar graphs summarize the power amplitude at the spatial frequency of 0.55 μm^{-1} (indicated by triangle) of sham versus post-MI groups as indicated. Figure 5A shows corresponding representative co-immunofluorescence images.

Cav3: The Cav3 power spectrum at 4pMI was upward shifted consistent with a more heterogeneous distribution while protein expression is significantly increased. The peak amplitude at the spatial frequency of 0.55 μm^{-1} indicated by triangle was significantly decreased indicating a loss of striation-associated Cav3 clusters.

RyR2: The RyR2 power spectrum was changed at 4pMI compared to sham showing a significantly reduced amplitude at the spatial frequency of 0.55 μm^{-1} indicated by triangle. The decreased peak signal together with increased signal between periodic peaks suggests a loss of RyR2 clusters at striations post-MI, possibly due to spatial reorganization since RyR2 protein expression was unchanged.

Jph2: The power versus frequency function was downward shifted at 8pMI, while protein expression was significantly decreased post-MI. In addition, the spatial frequency at 0.55 μm^{-1} indicated by triangle was significantly decreased consistent with a loss of Jph2 clusters at striations.

*, $p<0.05$.

Online Figure VIII

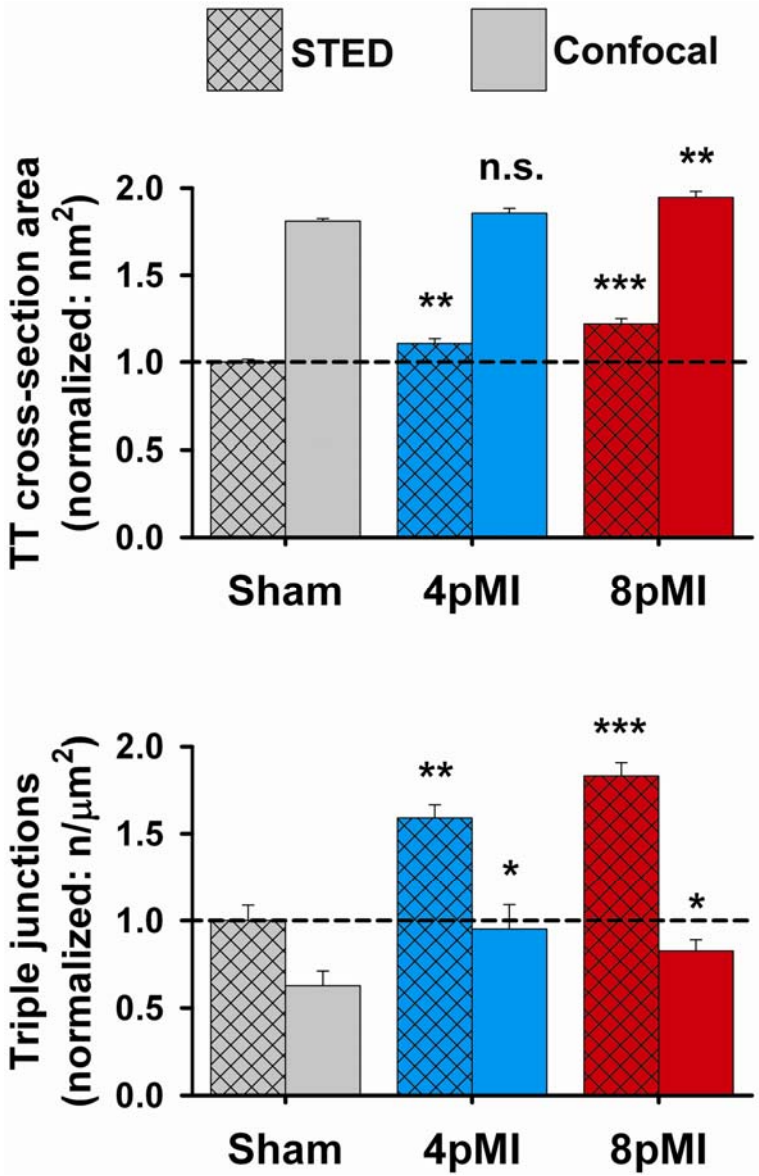

Online Figure VIII

Direct comparison of STED and confocal measurements of TT subresolution structures to estimate the detection sensitivity for nanometric post-MI changes.

All measurements were performed using the same optical microscopy system as described in Online Figure I-A.

Top: TT cross-sections dimensions were analyzed by 2D FWHM algorithm for the same sample TT samples of the indicated treatment groups (numbers as given by Table 2). STED measured significantly smaller TT cross-section dimensions in sham cardiomyocytes confirming the results shown in Figure 2 from untreated control cells. Despite significantly smaller TT dimensions, only STED detects a highly significant increase of the cross-section area at 4pMI, the early HF time point, a relatively subtle disease change clearly not resolved by confocal measurements. While confocal measurements detect a significant mean area increase at 8pMI (+7%), the relative increase measured versus sham is highly significantly larger for STED measurements (+22%; $p<10^{-40}$ versus confocal group at 8pMI).

Bottom: Triple junctions or TT bifurcations were analyzed by direct automated image quantification (see methods) as an indicator of network complexity. The normalized data show a dramatic increase of the number of triple junctions relative to sham at 8pMI, yet this progressive post-MI increase is only detected by STED, whereas the confocal data shows a tendency for a relative decrease at 8pMI. For image examples of TT network complexity please refer to Figures 3C and 4A.

*, $p<0.05$; **, $p<0.001$; ***, $p<0.0001$ each versus corresponding sham group; only changes versus sham are indicated for clarity. STED: hatched bars; confocal: open bars.

D. Supplemental References

1. Lehnart SE, Wehrens XH, Reiken S, Warrier S, Belevych AE, Harvey RD, Richter W, Jin SL, Conti M, Marks AR. Phosphodiesterase 4D deficiency in the ryanodine-receptor complex promotes heart failure and arrhythmias. *Cell.* 2005;123(1):25-35.

2. Chen Q, Williams R, Healy CL, Wright CD, Wu SC, O'Connell TD. An association between gene expression and better survival in female mice following myocardial infarction. *J Mol Cell Cardiol.*49(5):801-811.

3. Wu JC, Nasseri BA, Bloch KD, Picard MH, Scherrer-Crosbie M. Influence of sex on ventricular remodeling after myocardial infarction in mice. *J Am Soc Echocardiogr.* 2003;16(11):1158-1162.

4. Piro M, Della Bona R, Abbate A, Biasucci LM, Crea F. Sex-related differences in myocardial remodeling. *J Am Coll Cardiol.*55(11):1057-1065.

5. Cavasin MA, Tao Z, Menon S, Yang XP. Gender differences in cardiac function during early remodeling after acute myocardial infarction in mice. *Life Sci.* 2004;75(18):2181-2192.

6. Shioura KM, Geenen DL, Goldspink PH. Sex-related changes in cardiac function following myocardial infarction in mice. *Am J Physiol Regul Integr Comp Physiol.* 2008;295(2):R528-534.

7. Eggeling C, Ringemann C, Medda R, Schwarzmann G, Sandhoff K, Polyakova S, Belov VN, Hein B, von Middendorff C, Schonle A, Hell SW. Direct observation of the nanoscale dynamics of membrane lipids in a living cell. *Nature.* 2009;457(7233):1159-1162.

8. Nock R, Nielsen F. Statistical region merging. *IEEE Trans Pattern Anal Mach Intell.* 2004;26(11):1452-1458.

9. Liu ZQ. Scale space approach to directional analysis of images. *Appl Opt.* 1991;30(11):1369-1373.

10. Song LS, Sobie EA, McCulle S, Lederer WJ, Balke CW, Cheng H. Orphaned ryanodine receptors in the failing heart. *Proc Natl Acad Sci U S A.* 2006;103(11):4305-4310.

11. Louch WE, Mork HK, Sexton J, Stromme TA, Laake P, Sjaastad I, Sejersted OM. T-tubule disorganization and reduced synchrony of Ca2+ release in murine cardiomyocytes following myocardial infarction. *J Physiol.* 2006;574(Pt 2):519-533.

12. Williams GSB, Chikando AC, Tuan HTM, Sobie EA, Lederer WJ, Jafri MS. Dynamics of calcium sparks and calcium leak in the heart. *Biophys J.* 2011;101(6):1287-1296.

13. Hasenfuss G, Schillinger W, Lehnart SE, Preuss M, Pieske B, Maier LS, Prestle J, Minami K, Just H. Relationship between Na+-Ca2+-exchanger protein levels and diastolic function of failing human myocardium. *Circulation.* 1999;99(5):641-648.

14. Meyer M, Schillinger W, Pieske B, Holubarsch C, Heilmann C, Posival H, Kuwajima G, Mikoshiba K, Just H, Hasenfuss G, et al. Alterations of sarcoplasmic reticulum proteins in failing human dilated cardiomyopathy. *Circulation.* 1995;92(4):778-784.

15. He J, Conklin MW, Foell JD, Wolff MR, Haworth RA, Coronado R, Kamp TJ. Reduction in density of transverse tubules and L-type Ca(2+) channels in canine tachycardia-induced heart failure. *Cardiovasc Res.* 2001;49(2):298-307.

16. Balijepalli RC, Lokuta AJ, Maertz NA, Buck JM, Haworth RA, Valdivia HH, Kamp TJ. Depletion of T-tubules and specific subcellular changes in sarcolemmal proteins in tachycardia-induced heart failure. *Cardiovasc Res.* 2003;59(1):67-77.

17. Heinzel FR, Bito V, Biesmans L, Wu M, Detre E, von Wegner F, Claus P, Dymarkowski S, Maes F, Bogaert J, Rademakers F, D'Hooge J, Sipido K. Remodeling of T-tubules and reduced synchrony of Ca2+ release in myocytes from chronically ischemic myocardium. *Circ Res.* 2008;102(3):338-346.

18. Lyon AR, MacLeod KT, Zhang Y, Garcia E, Kanda GK, Lab MJ, Korchev YE, Harding SE, Gorelik J. Loss of T-tubules and other changes to surface topography in ventricular

myocytes from failing human and rat heart. *Proc Natl Acad Sci U S A.* 2009;106(16):6854-6859.

19. Ibrahim M, Al Masri A, Navaratnarajah M, Siedlecka U, Soppa GK, Moshkov A, Al-Saud SA, Gorelik J, Yacoub MH, Terracciano CM. Prolonged mechanical unloading affects cardiomyocyte excitation-contraction coupling, transverse-tubule structure, and the cell surface. *FASEB J.*24(9):3321-3329.

20. Wei S, Guo A, Chen B, Kutschke W, Xie YP, Zimmerman K, Weiss RM, Anderson ME, Cheng H, Song LS. T-tubule remodeling during transition from hypertrophy to heart failure. *Circ Res.*107(4):520-531.

21. van Oort RJ, Garbino A, Wang W, Dixit SS, Landstrom AP, Gaur N, De Almeida AC, Skapura DG, Rudy Y, Burns AR, Ackerman MJ, Wehrens XH. Disrupted junctional membrane complexes and hyperactive ryanodine receptors after acute junctophilin knockdown in mice. *Circulation.*123(2011, 9):979-988.

22. Wu CY, Jia Z, Wang W, Ballou LM, Jiang YP, Chen B, Mathias RT, Cohen IS, Song LS, Entcheva E, Lin RZ. PI3Ks maintain the structural integrity of T-tubules in cardiac myocytes. *PLoS One.*6(9):e24404.

23. Kemi OJ, Hoydal MA, Macquaide N, Haram PM, Koch LG, Britton SL, Ellingsen O, Smith GL, Wisloff U. The effect of exercise training on transverse tubules in normal, remodeled, and reverse remodeled hearts. *J Cell Physiol.*226(9):2235-2243.

24. Sachse FB, Torres NS, Savio-Galimberti E, Aiba T, Kass DA, Tomaselli GF, Bridge JH. Subcellular structures and function of myocytes impaired during heart failure are restored by cardiac resynchronization therapy. *Circ Res.*110(4):588-597.

25. Maron BJ, Ferrans VJ, Roberts WC. Ultrastructural features of degenerated cardiac muscle cells in patients with cardiac hypertrophy. *Am J Pathol.* 1975;79(3):387-434.

26. Schaper J, Froede R, Hein S, Buck A, Hashizume H, Speiser B, Friedl A, Bleese N. Impairment of the myocardial ultrastructure and changes of the cytoskeleton in dilated cardiomyopathy. *Circulation.* 1991;83(2):504-514.

27. Kostin S, Scholz D, Shimada T, Maeno Y, Mollnau H, Hein S, Schaper J. The internal and external protein scaffold of the T-tubular system in cardiomyocytes. *Cell Tissue Res.* 1998;294(3):449-460.

28. Kaprielian RR, Stevenson S, Rothery SM, Cullen MJ, Severs NJ. Distinct patterns of dystrophin organization in myocyte sarcolemma and transverse tubules of normal and diseased human myocardium. *Circulation.* 2000;101(22):2586-2594.

29. Louch WE, Bito V, Heinzel FR, Macianskiene R, Vanhaecke J, Flameng W, Mubagwa K, Sipido KR. Reduced synchrony of Ca2+ release with loss of T-tubules-a comparison to Ca2+ release in human failing cardiomyocytes. *Cardiovasc Res.* 2004;62(1):63-73.

30. Cannell MB, Crossman DJ, Soeller C. Effect of changes in action potential spike configuration, junctional sarcoplasmic reticulum micro-architecture and altered t-tubule structure in human heart failure. *J Muscle Res Cell Motil.* 2006;27(5-7):297-306.

31. Crossman DJ, Ruygrok PN, Soeller C, Cannell MB. Changes in the organization of excitation-contraction coupling structures in failing human heart. *PLoS One.*6(3):e17901.